

ENSO Modulation of the Interannual and Intraseasonal Variability of the East Asian Monsoon—A Model Study

NGAR-CHEUNG LAU AND MARY JO NATH

NOAA/Geophysical Fluid Dynamics Laboratory, Princeton University, Princeton, New Jersey

(Manuscript received 1 September 2005, in final form 14 December 2005)

ABSTRACT

The impacts of ENSO on the evolution of the East Asian monsoon have been studied using output from a general circulation model experiment. Observed monthly variations of the sea surface temperature (SST) field have been prescribed in the tropical eastern and central Pacific, whereas the atmosphere has been coupled to an oceanic mixed layer model beyond this forcing region. During the boreal summer of typical El Niño events, a low-level cyclonic anomaly is simulated over the North Pacific in response to enhanced condensational heating over the equatorial central Pacific. Advective processes associated with the cyclone anomaly lead to temperature tendencies that set the stage for the abrupt establishment of a strong Philippine Sea anticyclone (PSAC) anomaly in the autumn. The synoptic development during the onset of the PSAC anomaly is similar to that accompanying cold-air surges over East Asia.

The air–sea interactions accompanying the intraseasonal variations (ISV) in the model atmosphere exhibit a strong seasonal dependence. During the summer, the climatological monsoon trough over the subtropical western Pacific facilitates positive feedbacks between the atmospheric and oceanic fluctuations. Conversely, the prevalent northeasterly monsoon over this region in the winter leads to negative feedbacks. The onset of the PSAC anomaly is seen to be coincident with a prominent episode of the leading ISV mode. The ENSO events could influence the amplitude of the ISV by modulating the large-scale flow environment in which the ISV are embedded. Amplification of the summer monsoon trough over the western Pacific during El Niño enhances air–sea feedbacks on intraseasonal time scales, thereby raising the amplitudes of the ISV. A weakening of the northeasterly monsoon in El Niño winters suppresses the frequency and strength of the cold-air surges associated with the leading ISV mode in that season.

Many aspects of the model simulation of the relationships between ENSO and the East Asian monsoon are in agreement with observational findings.

1. Introduction

Our empirical knowledge of the observed East Asian monsoon (EAM), including its seasonal characteristics, interannual variability, and interactions with various phenomena in the coupled atmosphere–ocean system, has recently been summarized in a monograph edited by Chang (2004). Several chapters in that publication (K.-M. Lau et al. 2004; Wang and Li 2004; Huang et al. 2004) contain surveys of the observational evidence of, and physical processes contributing to, the relationships between El Niño–Southern Oscillation (ENSO) events and fluctuations of the EAM. These reviews are built upon cumulative findings reported earlier by Li (1990),

Zhang et al. (1996), Chang et al. (2000a, 2000b), Wang et al. (2000), Wang and Zhang (2002), and many others. It has been noted in these studies that many ENSO-related circulation changes over East Asia are linked to the evolution of the Philippine Sea anticyclone (PSAC) anomaly in the lower troposphere. Such investigations also reveal the substantial roles of remote ENSO forcing, in situ air–sea coupling, and intraseasonal variations in different stages of the PSAC development.

It is well recognized that the strength and polarity of the PSAC anomaly exert a strong influence on East Asian climate. During the boreal winter, a strong positive PSAC anomaly (which typically occurs during the mature phase of El Niño events) is accompanied by southwesterly surface wind anomalies on its northwestern flank. This circulation change is in opposition to the climatological northeasterly flow over East Asia. The resulting weakening of the wintertime EAM leads to

Corresponding author address: Ngar-Cheung Lau, GFDL/NOAA Princeton University, P.O. Box 308, Forrestal Campus U.S. Route 1, Princeton, NJ 08542.
E-mail: gabriel.lau@noaa.gov

above-normal temperature and precipitation in that region. In those instances when the PSAC anomaly persists through the following spring and early summer, it could also affect the intensity of the mei-yu and baiu rainbelts over eastern China and Japan, as well as the trajectories of tropical cyclones in the western Pacific. Improved understanding of the behavior of PSAC, as well as its interactions with other prominent modes of climate variability such as ENSO, is hence a goal of considerable importance in EAM research.

Efforts to simulate various aspects of EAM variability associated with ENSO, and to delineate the underlying mechanisms responsible for such observed relationships, have been made using general circulation models (GCMs). Results from these model studies have also been reviewed in the aforementioned monograph (see chapters by N.-C. Lau et al. 2004, hereafter LN04; Kang 2004; Sumi et al. 2004). Specifically, Lau and Nath (2000) have demonstrated that the ENSO modulation of PSAC and the accompanying precipitation changes can be replicated in a model atmosphere with a reasonable degree of fidelity. More detailed findings on the simulated PSAC development from the late boreal autumn of the ENSO year to the following spring were presented by LN04. These model diagnostics were primarily motivated by the corresponding observational study by Wang et al. (2000). Evidence has been shown in Wang et al. (2000) and LN04 associating the PSAC anomaly with the remote atmospheric Rossby wave response to the altered condensational heating over the equatorial western Pacific during ENSO episodes. It has been further illustrated in both studies that, after the PSAC anomaly is fully established in the boreal winter and spring, it could affect the heat transfer across the local air-sea interface through changes in wind speed, low-level air temperature and humidity, and cloud cover. The ensuing modification of the sea surface temperature (SST) conditions in the subtropical western Pacific could in turn influence the overlying atmospheric circulation. Such air-sea feedbacks contribute to the maintenance of the PSAC anomaly, as well as to its eastward displacement over the western Pacific during the spring season after the ENSO year.

Wang and Zhang (2002, hereafter WZ02) have conducted another observational study that is complementary to the earlier investigation of Wang et al. (2000). The more recent work is focused on the favorable atmospheric preconditions in the EAM region in the summer and early autumn leading to the onset of the PSAC anomaly, and the characteristics of intraseasonal variations (ISV) in different stages of its development. These authors noted that the ISV are closely related to

the establishment of the PSAC anomaly, and that local air-sea interactions play an essential role in the evolution of these ISV. The nature of such air-sea coupling is seen to exhibit a strong seasonal dependence on the climatological flow pattern in which the ISV are embedded. The findings in WZ02, in conjunction with those in Wang et al. (2000), provide a comprehensive account of the phenomena and processes attending the entire life history of the observed PSAC anomaly. Of particular interest in this evolution are the antecedent phase in the summer of the ENSO year, the establishment phase in the autumn, and the growth and maintenance phase in the following winter and spring.

The observational results reported by WZ02 have given us fresh incentives to examine GCM simulation of the circulation changes in the EAM region prior to the formation of the PSAC anomaly, the typical synoptic development during the onset stage of this anomaly, and the attendant ISV behavior. Our previous investigations on ENSO-EAM relationships were mostly concerned with simulated atmosphere-ocean variations on monthly time scales *after* the PSAC anomaly is established. By devoting our attention in the present study to the features and mechanisms *before* and *during* PSAC onset, as well as to the role of ISV in PSAC development, we strive to offer a more complete documentation of the ENSO-related variability over the EAM region in the model atmosphere. The present work may hence be viewed as a complement to the model diagnoses of Lau and Nath (2000) and LN04, in much the same fashion that the observational study of WZ02 serves to augment the earlier work of Wang et al. (2000).

After a brief account of the experimental design in section 2, the salient atmospheric and oceanic changes in the EAM region in the course of typical El Niño and La Niña events are reviewed in section 3. The role of remote ENSO forcing from the equatorial central Pacific in setting up the large-scale circulation pattern over East Asia during the boreal summer, as well as the accompanying meteorological factors that are favorable for the subsequent initiation of the PSAC anomaly, are examined in section 4. The typical synoptic features associated with the abrupt onset of the PSAC anomaly in autumn are identified in section 5. The space-time characteristics of the principal ISV mode in various seasons are documented in section 6. Section 7 is devoted to examining the dependence of the ISV in different seasons on air-sea feedbacks as modulated by ENSO signatures in the background flow. Section 8 contains a summary and discussion of the principal findings.

2. Description of GCM experiment and analysis procedures

The model dataset analyzed in this study is identical to that produced in one of the experiments described in LNW04. The atmospheric GCM used in these experiments is a spectral global model with a rhomboidal truncation at 30 wavenumbers (with equivalent horizontal resolution of 3.75° in longitude and $\sim 2.2^\circ$ in latitude) and with 14 sigma levels in the vertical direction. Detailed documentation of the numerics and physics of this model tool has been provided by Gordon and Stern (1982) and Broccoli and Manabe (1992). In particular, precipitation processes are parameterized using the moist convective adjustment scheme designed by Manabe et al. (1965). The model climatologies of precipitation and near-surface circulation in various seasons have been compared with observations by LNW04 (see their Fig. 1). Standard circulation statistics of the output from this model have been compiled by Alexander and Scott (1995).

Within the central-eastern Pacific zone between 15°S and 15°N , and from 172°E eastward to the South American coast, observed monthly SST variations have been inserted in the lower boundary condition of the GCM throughout the 1950–99 period. At all ice-free oceanic grid points outside of this forcing domain, the GCM has been coupled to a one-dimensional oceanic mixed layer model (MLM) with variable depth. The MLM is similar to that formulated by Gaspar (1988), and the procedure for coupling this model to the atmospheric GCM has been described by Alexander et al. (2000). Fluctuations in the mixed layer temperature at each grid point are driven by local flux exchanges across the air–sea interface, which could be linked to remote influences of ENSO. These oceanic temperature changes could in turn affect the atmospheric conditions aloft. The setup in such model runs (labeled as the “MLM” experiment in LNW04) incorporates the forcing of the global atmosphere by ENSO-related SST changes prescribed in the near-equatorial central and eastern Pacific, as well as simplified two-way interactions between this atmospheric response and the underlying ocean beyond the forcing region. This experimental design hence facilitates a comprehensive investigation of the effects of both remote changes in the tropical Pacific east of the date line and in situ air–sea coupling within the EAM region on the family of monsoonal phenomena reviewed in the introductory section. The long-term-averaged temperature of the simulated mixed layer has been constrained to follow the observed conditions by using the flux adjustment technique described by Manabe et al. (1991). Altogether 16

integrations have been conducted, with each 50-yr run being initiated from independent atmospheric conditions. Unless otherwise stated, the results shown in the present study are based on averages over the 16 members of this ensemble.

The statistical significance of the signals appearing in the composite patterns to be presented in the following sections has been assessed using the two-tailed Student's *t*-test. Features that surpass the 90%, 95%, or 99% confidence levels are highlighted, as explained in the captions of the individual figures.

3. Evolution of the PSAC anomaly during ENSO events

We shall focus our attention on the typical behavior of the EAM during the prominent El Niño episodes starting in 1957, 1965, 1972, 1982, 1991, and 1997, and the La Niña events starting in 1955, 1970, 1973, 1975, 1988, and 1998. This selected set of ENSO events is nearly identical to that examined by WZ02, so that our model results may be compared directly with the observations presented in that study. We henceforth refer to a year of strong ENSO development as “Year (0),” and the year after as “Year (1).” A specific period in the ENSO cycle is denoted by a character string consisting of either the first three letters of a given month or the first letter of several successive months, followed by the year label (0 or 1) in parentheses. For instance, the October–November–December period of Year (0) is OND (0). Averages taken over the six El Niño and six La Niña events are labeled as “warm composites” and “cold composites,” respectively. Differences between these two composites are called “warm minus cold composites.”

The warm minus cold composites of the sea level pressure (SLP) and precipitation fields are displayed in Fig. 1 using contours and shading, respectively, for the OND (0) period. Results are presented using the ensemble averages generated in the MLM experiment (left panel) and the observational reanalysis products of the National Centers for Environmental Prediction–National Center for Atmospheric Research (NCEP–NCAR). Both the observed and simulated patterns indicate the presence of a high SLP anomaly over the South China and Philippine Seas. The simulated anticyclonic center is displaced to the west of its observed counterpart. Below-normal precipitation prevails in this high pressure zone and along the equatorial western Pacific between 120° and 150°E , whereas wet conditions are discernible to the northwest of the PSAC anomaly. These precipitation anomalies are discernible in both model and NCEP–NCAR patterns, as well as in

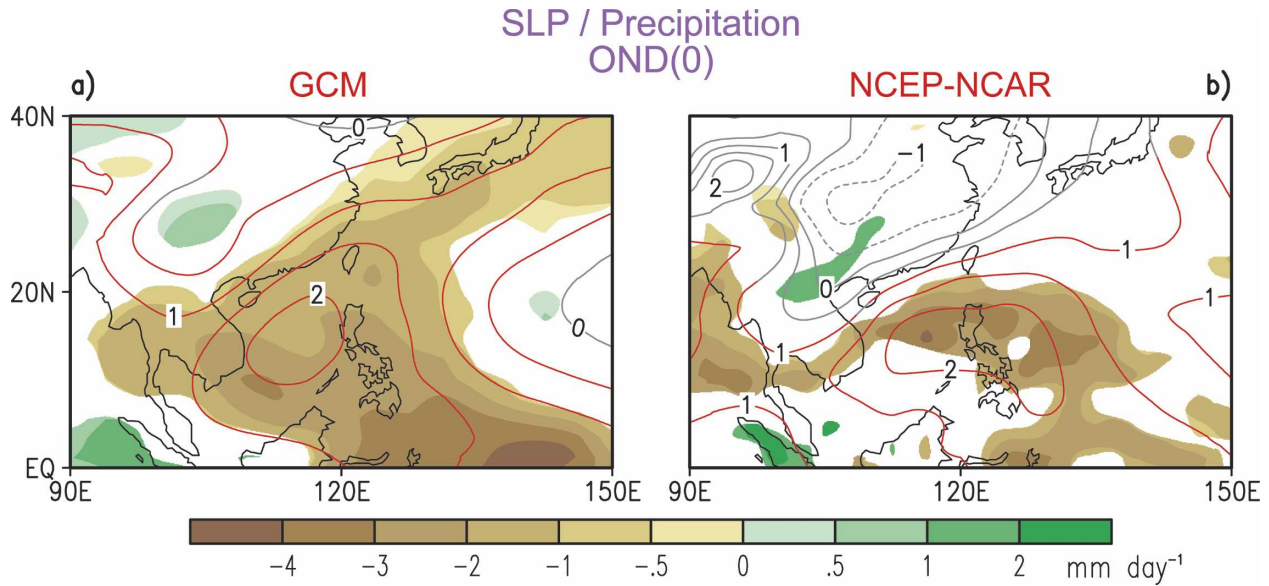


FIG. 1. Warm minus cold composites of SLP (contours; interval: 0.5 mb) and precipitation (shading; see scale bar at bottom) for the OND (0) period, as computed using (a) GCM data and (b) NCEP–NCAR reanalyses. Red contours indicate positive SLP anomalies surpassing the 90% significance level. Gray contours represent SLP anomalies (both positive and negative) below the 90% level. Only precipitation anomalies above the 90% significance level are depicted by color shading.

composite charts presented by Lau and Wang (2006) based on observational estimates provided by the Global Precipitation Climatology Project (GPCP) for a smaller set of ENSO events.

The space–time development of the PSAC and the underlying oceanic changes in the course of a typical ENSO cycle is illustrated in Fig. 2, which shows variations of the composite anomalies of monthly averaged SLP (contours) and SST (shading) with longitude (abscissa) and temporal phase of ENSO (ordinate). These patterns are based on averages over the 10°–20°N zone. Results for the warm and cold composites are presented in the upper and lower panels, respectively. The left panels correspond to data from the GCM simulation. The right panels are based on observational estimates of the NCEP–NCAR reanalyses for SLP and Smith et al. (1996) for SST.

During El Niño events, both the observed and simulated distributions (see Figs. 2a and 2c) show the emergence of a positive SLP anomaly center in Oct (0) near 120°E. This feature intensifies as it migrates eastward in the following months. By Jan (1), it attains maximum amplitude and is centered near 135°E. The SLP anomaly is discernible through the middle of Year (1). Accompanying this evolution of the SLP field is a SST pattern with a distinct east–west contrast (see shading). Warm SST anomalies appear to the west of the high SLP center, whereas cold conditions prevail near and to the east of this center. This characteristic SST pattern

persists from late autumn of Year (0) through the summer of Year (1). The simulated SST anomalies (Fig. 2a) also exhibit a tendency to expand eastward with time. For a detailed interpretation of the above relationships between the SLP and SST anomalies, the readers are referred to Wang et al. (2000) and LNW04. Evidence has been presented in these works on the roles of the near-surface atmospheric circulation and cloud cover associated with the PSAC anomaly in modulating the surface heat and radiative fluxes, thereby altering the local SST conditions. These studies have also noted that the ensuing air–sea interactions in turn contribute to maintenance and eastward displacement of the SLP and SST anomalies.

The patterns in Figs. 2a and 2c further indicate that the PSAC signal is preceded by a negative SLP anomaly centered near 170°E in the boreal summer of Year (0). The implications of this low pressure anomaly on the summertime climate in the EAM region, as well as its link to ENSO forcing in the equatorial Pacific, will be addressed in the following sections.

The PSAC center in the model atmosphere (Fig. 2a) is shifted to the west of its observed position (Fig. 2c). The eastward migration of the observed PSAC anomaly is most apparent in Oct (0)–Nov (0), whereas the strongest displacement in the simulation occurs in Jan (1)–Feb (1). The zone separating the observed warm and cold SST anomalies is almost stationary at ~130°E through the first half of Year (1), whereas the

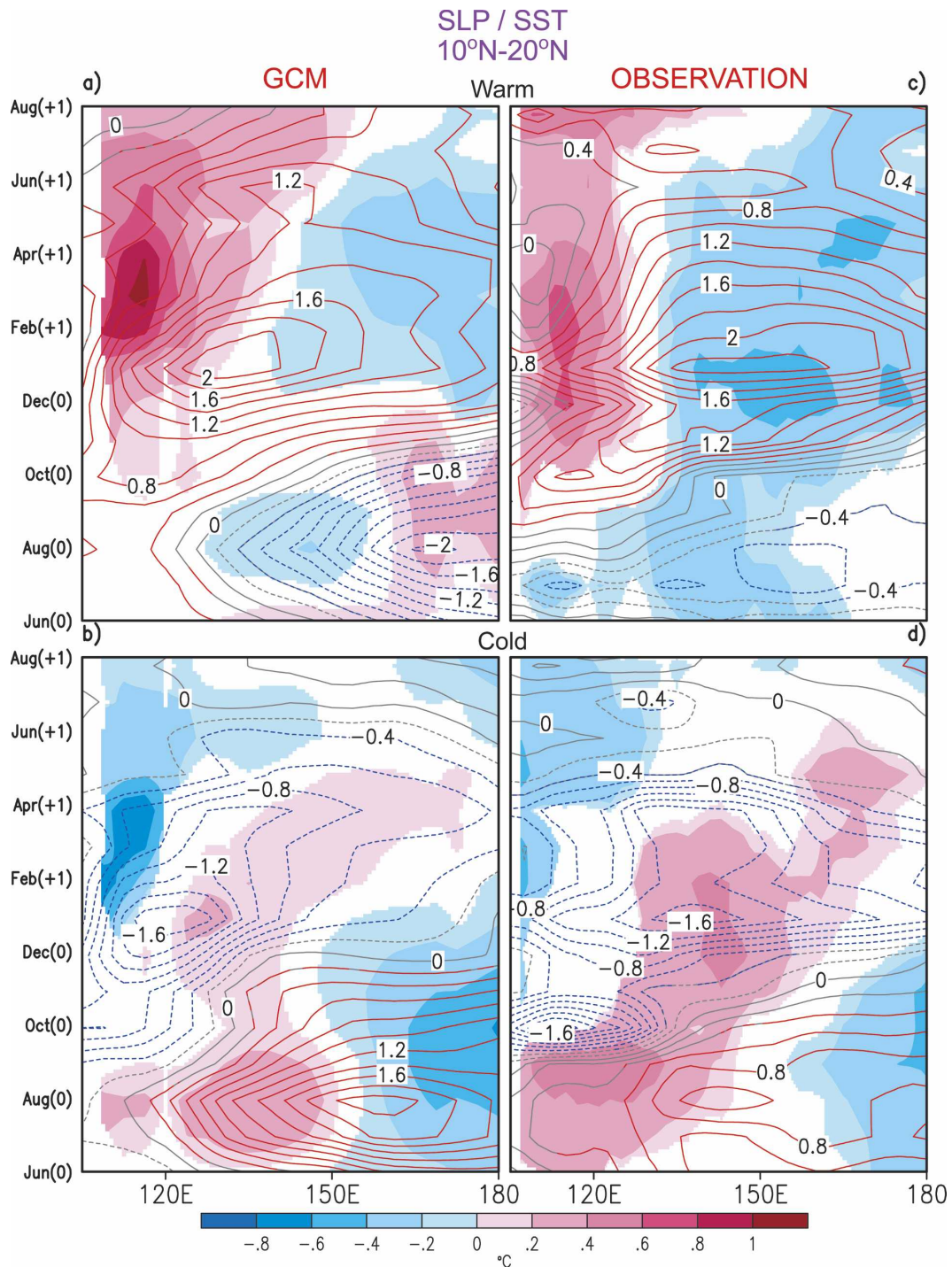


FIG. 2. Time-longitude variations of the (top) warm and (bottom) cold composites of anomalous SLP (contours; interval: 0.2 mb) and SST (shading; see scale bar at bottom) as computed using (left) GCM data and (right) observational estimates. Data values have been averaged over the 10°–20°N zone. Red (blue) contours indicate positive (negative) SLP anomalies surpassing the 95% significance level. Gray contours represent SLP anomalies below the 95% level. Only SST anomalies above the 95% significance level are depicted by color shading.

corresponding feature in the simulation is seen to advance eastward during the same period. The negative SLP anomaly near the date line during the summer of Year (0) in the model pattern is noticeably stronger than its observed counterpart.

Except for a sign reversal, the typical characteristics of the SLP and SST anomalies in La Niña events (Figs. 2b and 2d) are analogous to those in El Niño events. The timing of the principal SLP and SST signals is similar during both warm and cold ENSO episodes. Anomaly centers in the cold composite patterns are displaced to the west of their counterparts in the warm composites. This displacement is evidently linked to a corresponding westward shift of the negative precipitation anomaly over the central equatorial Pacific in cold events relative to the positive precipitation anomaly in warm events (not shown). Such nonlinearities in the circulation and precipitation signals during El Niño and La Niña episodes have previously been investigated by Hoerling et al. (1997). These authors noted that the asymmetry of the tropical precipitation forcing with respect to ENSO polarity might be attributed to the sensitivity of deep convection to the total, rather than the anomalous, value of the SST.

We proceed to examine the temporal development of the simulated SLP anomaly over the South China and Philippine Seas during individual ENSO events, and the degree of intersample variability of such development in the ensemble of 16 model runs conducted in this study. For each member of the ensemble, pentad (pd; 5 day) means of the SLP data averaged over the region extending from 10° to 20°N and from 105° to 135°E have been computed. We shall hereafter refer to these mean values as the “SLP index.” Low-frequency (LF) fluctuations were then retained by subjecting the data to a 7 pd running mean. In each pentad, the SLP index (expressed as a departure from the climatological annual average) for the 16 individual runs was rank ordered. The values corresponding to the 10th, 25th, 50th, 75th, and 90th percentiles of this population were then determined. The time variations of the 10th–25th, 25th–75th, and 75th–90th percentile ranges are displayed using shaded bands in Fig. 3 for the Sep (0)–May (1) period of each selected El Niño (left panel, see red shading) and La Niña (right panel, blue shading) event. The white curves embedded in these bands represent the 50th percentile (median) values. Superposed on the time series for individual events is the corresponding climatological seasonal march (dashed black curve), as obtained by averaging over the entire 1950–99 period and all 16 model runs. The results based on composites over all warm and all cold ENSO events are shown at the bottom of Figs. 3a and 3b, respectively.

The graphs in Fig. 3 illustrate that the median of the SLP index is above normal in every warm episode and below normal in every cold episode. During most of the El Niño events, the shaded bands in Fig. 3a lie above the climatological curve through much of the Nov (0)–Mar (1) period, indicating that more than 90% of the 16 individual runs yield positive SLP anomalies over the subtropical western Pacific. The degree of reproducibility of the SLP changes is comparatively lower in the cold events (Fig. 3b), with typically 75%–90% of the population lying below the climatological mean.

In view of the considerable linearity of the primary signals in Figs. 2–3 with respect to the polarity of the ENSO forcing, we shall henceforth discuss our results mostly in terms of atmospheric and oceanic changes occurring in El Niño events, with the understanding that the sign of these anomalies would be reversed in La Niña episodes.

4. Precursory atmospheric conditions in the summer of Year (0)

WZ02 have identified several aspects of the observed atmospheric environment in the boreal summer of Year (0) that are favorable for the formation of the SLP anomaly over the Philippine Sea several months later. The ability of the GCM to reproduce such preconditions is examined in this section. The warm minus cold composites of the GCM-simulated horizontal wind vector at 200 and 850 mb during the Jun (0)–Sep (0) period [JJAS (0)] are presented in the left panels of Fig. 4. The anomalous flow pattern in the upper troposphere (Fig. 4a) is dominated by an anticyclone centered near 20°N, 170°E, and a cyclone over northeastern China. This model pattern is in general agreement with the observations (see Fig. 8a of WZ02). Over the North Pacific, a cyclonic anomaly at 850 mb (Fig. 4b) is simulated underneath the upper-level anticyclone. This cyclonic feature in the lower troposphere coincides with the prominent negative SLP anomaly over the western subtropical Pacific in the summer of Year (0) (Fig. 2a), and is too strong when compared with the observed pattern (see Fig. 8b of WZ02).

We next consider the role of ENSO-related forcing from the equatorial Pacific in generating the circulation anomalies seen in Figs. 4a–4b. The methodology adopted here is similar to that used in Wang et al. (2003), LNW04, and Lau and Wang (2006). The effects of a certain forcing on the atmosphere are identified by prescribing that forcing in a stationary wave model (SWM), and then examining the steady-state model response. In the present application, the SWM developed by Ting and Yu (1998) has been employed. The nu-

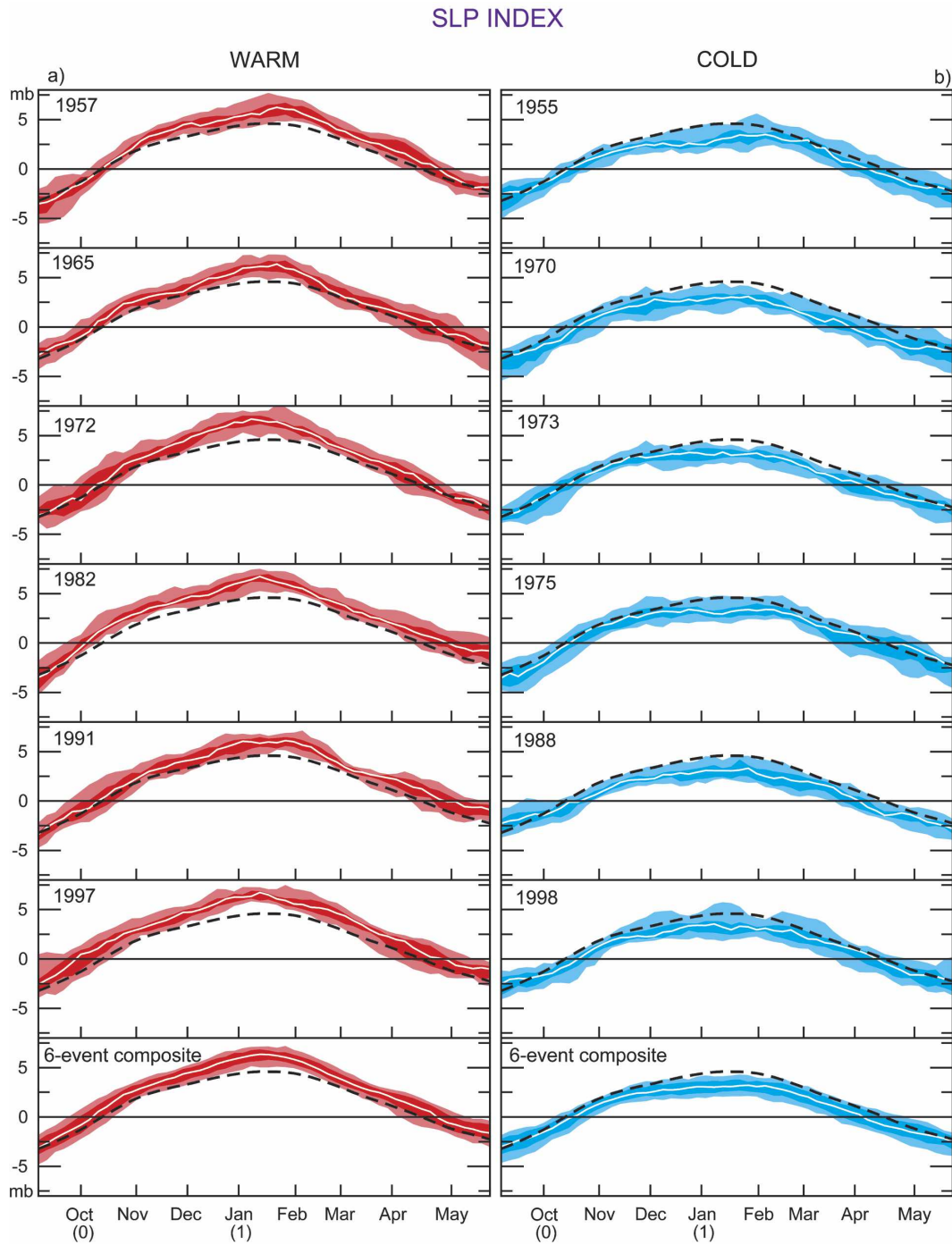


FIG. 3. Time series of the low-frequency component of the anomalous SLP averaged over the 10° – 20° N, 105° – 135° E region, as computed using GCM output for the (left) six individual warm events and the six-event composite and for the (right) six individual cold events and the six-event composite. Dense color shading indicates the range between the 25th and 75th percentiles in the population of 16 realizations generated in the ensemble experiment, whereas lighter color shading indicates the 10th–25th and 75th–90th percentile ranges. The temporal variation of the median (50th percentile) values of the SLP index is depicted by the white curves embedded in the shaded bands. The dashed black curve in each panel depicts the climatological variation of the SLP Index.

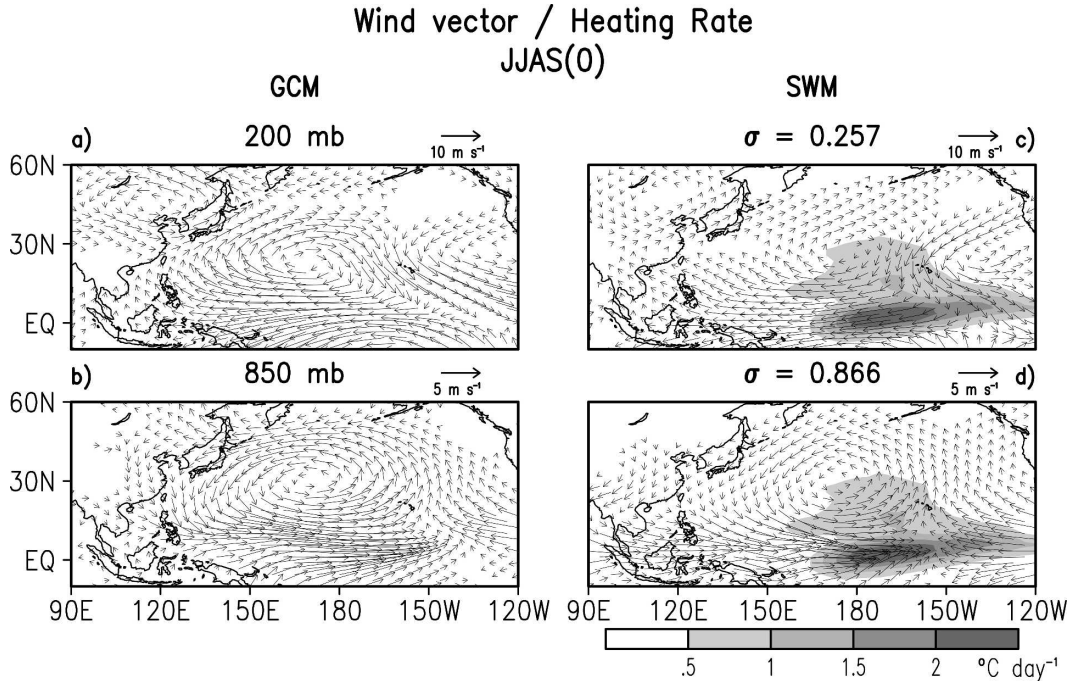


FIG. 4. Warm minus cold composites of the vector wind field at (a) 200 and (b) 850 mb, as computed using GCM data for the JJAS (0) period. Steady-state solution of the vector wind field at sigma levels of (c) 0.257 and (d) 0.866, as computed using the stationary wave model subjected to diabatic heating in the tropical central Pacific (shading; see scale bar at bottom right). Scales for wind vectors are shown at the upper right of individual panels.

merical framework of this model resembles that of the GCM for the MLM experiment. The SWM used a three-dimensional basic state, which corresponds to the GCM climatology for the JJAS season. The anomalous diabatic heating and cooling in the tropical Pacific have been used as forcing terms in the SWM. The three-dimensional structure of this forcing has been obtained using the warm minus cold composite of the heating rates, as simulated in the MLM experiment during the JJAS (0) period. The horizontal distribution of the diabatic forcing (not shown) is characterized by a dipolar pattern, with a cooling center over the western tropical Pacific and a heating center in the eastern/central Pacific. This configuration is associated with the eastward displacement of the Walker circulation in El Niño events. Solutions of the SWM have been obtained by combining the effects of both the cooling and heating centers, as well as by considering the cooling and heating centers separately. Over the Pacific Basin, the response to the combination of cooling and heating centers (not shown) bears a strong resemblance to that forced by the heating center only, thus indicating the dominant influence of the latter feature on the circulation in that region.

The steady-state solution of the SWM, when subjected to positive heating in the central tropical Pacific

only, is portrayed using wind vectors at the sigma levels of 0.257 (Figs. 4c) and 0.866 (Fig. 4d). The distribution of the vertically integrated heating rates is depicted by shading in both panels. The strong similarities between the SWM solution and the full GCM data confirm that the circulation anomalies noted in Figs. 4a–4b may be attributed to variations in the heat source in the central and eastern tropical Pacific during ENSO episodes. These anomalies are reminiscent of the Rossby wave pattern forced by a center of low-level convergence at the equator, as shown by Matsuno (1966) and Gill (1980).

Steady-state solutions have also been obtained by subjecting the SWM to cooling centered near 150°E . These results [not shown, but see Fig. 6a of Lau and Wang (2006)] indicate that this cold source mainly affects the circulation over South Asia, whereas the signals in the Pacific sector are much weaker than the responses to the heating east of the date line (Figs. 4c–4d).

Influences of the anomalous flow patterns in Fig. 4 on the atmospheric environment may be inferred from the tendencies resulting from various advective processes associated with these patterns. The effects of the low-level cyclonic anomaly on the summertime temperature conditions in the EAM region are delineated in Fig. 5.

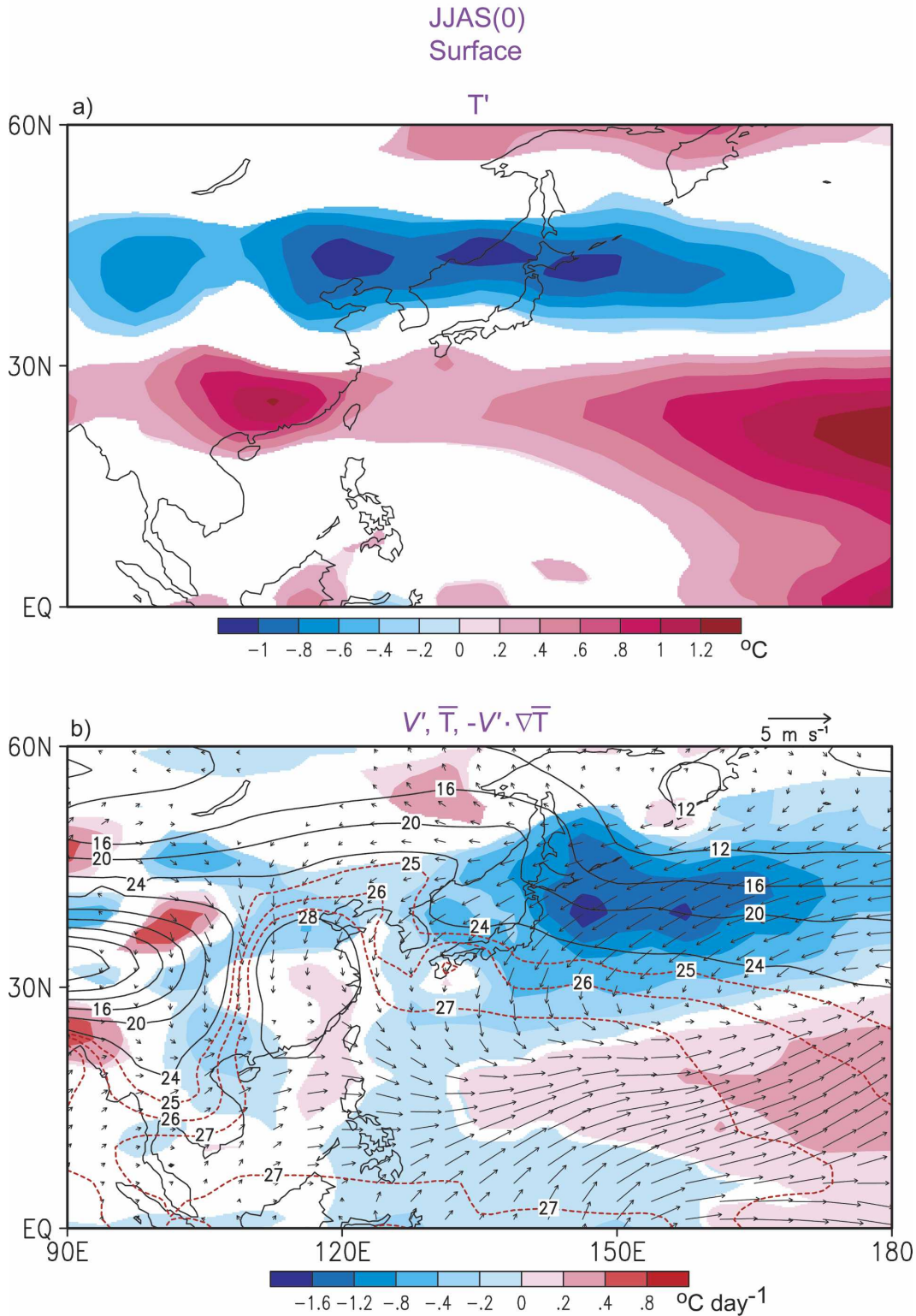


FIG. 5. Distributions of (a) warm minus cold composites of surface air temperature (shading, see scale bar at bottom) and (b) climatological surface air temperature (contours; interval for solid contours: 4°C), as well as warm minus cold composites of surface wind vector (arrows; see scale at upper right) and advection of the climatological temperature by the anomalous wind vector (shading; see scale bar at bottom). All computations are based on GCM data for the JJAS season (climatological temperature) and the JJAS (0) period (composite fields). Only anomalies of temperature and temperature advection above the 95% significance level are depicted by color shading.

The distribution of the warm minus cold composite of the surface air temperature (SAT) is plotted in the upper panel. The lower panel shows the climatological SAT for the JJAS season (\bar{T} , contours), as well as the warm minus cold composites of the surface wind vector (\mathbf{V}' , arrows) and the horizontal advection of climatological temperature by the anomalous flow ($-\mathbf{V}' \cdot \nabla \bar{T}$, shading). The composite data are based on the JJAS (0) period. The most prominent feature in Fig. 5a is the belt of below-normal SAT between 30° and 50°N , and extending eastward from northern China to the western Pacific. The cool conditions in the temperate zone of East Asia during the summer of El Niño years have been observed by many investigators (see WZ02 and references therein). WZ02 have further noted that the presence of this cold anomaly, in conjunction with the strengthened upper-level trough over northeastern Asia (see Figs. 4a and 4c), set the stage for more frequent and intense southward invasion of cold air masses toward the subtropical western Pacific in the following months. Such enhanced cold-air activities are conducive to the establishment of the PSAC anomaly in the autumn of Year (0) (see section 3 of WZ02 and section 5 herein).

In Fig. 5b, the low-level cyclone anomaly centered near the date line is seen to be accompanied by northeasterlies over the extratropical western Pacific, and northerlies over eastern China and the nearby waters. These anomalous wind vectors are oriented from maritime or high-latitude regions with relatively cold mean temperatures to warmer sites in eastern China and the subtropics (see contours in Fig. 5b). Cold temperature advection ($-\mathbf{V}' \cdot \nabla \bar{T} < 0$) prevails along a broad zone between 30° and 50°N (see shading in Fig. 5b), which bears some spatial correspondence with the eastern portion of the negative SAT anomaly in Fig. 5a. Hence, the cold condition over northeastern Asia during the summer of El Niño is partially due to temperature advection by the anomalous North Pacific cyclone. The contribution of this advective process to the below-normal temperature west of $\sim 110^\circ\text{E}$ is less evident.

The pattern for the advection of the anomalous temperature by the climatological flow ($-\bar{\mathbf{V}} \cdot \nabla T'$, not shown) is much weaker and less organized than that for $-\mathbf{V}' \cdot \nabla \bar{T}$ in Fig. 5b.

5. Synoptic development during onset of PSAC anomaly

WZ02 has described the synoptic circumstances in the establishment stage of the observed PSAC anomaly by compositing various atmospheric fields relative to the onset dates of this phenomenon for individual El

Niño events. An analogous analysis procedure is applied here to the model output. For each of the 16 realizations of the 6 individual strong El Niño events (i.e., a total of 96 samples), the time series of the anomalous SLP index for the South China and Philippine Seas (see definition in section 3) was examined. The LF component of these time series was obtained by performing a running mean over 7 pd. The approximate time of occurrence (denoted as pentad \bar{O}) of the establishment phase is identified for a given sample if the LF component of the time series for that sample satisfies the following criteria, which are developed in accordance with the observational evidence presented in WZ02 as follows:

- (i) The \bar{O} falls within the Sep (0)–Oct (0) period.
- (ii) The anomalous SLP index is negative in each of the 3 pd prior to \bar{O} ; the average of this anomalous index over the 3 pd after \bar{O} , minus the corresponding average over the 3 pd prior to \bar{O} , exceeds +1 mb.
- (iii) The anomalous SLP index remains positive for each of the 24 pd after \bar{O} ; the average of this anomalous index over the 24 pd after \bar{O} exceeds +1 mb.

Out of the 96-sample time series available, we have identified 25 cases in which the temporal evolution of the SLP index conforms to the above criteria. The typical time of occurrence of the PSAC onset in the model atmosphere, as inferred from the average of \bar{O} over the latter cases, is the pentad of 3–7 October. The number of cases selected from the 1957, 1965, 1972, 1982, 1991, and 1997 events is 5, 2, 8, 4, 4, and 2, respectively. Of the remaining $96 - 25 = 71$ samples that do not meet all three criteria listed above, 26 cases satisfy criteria (i) and (ii), but not (iii); 34 cases satisfy (i) and (iii), but not (ii); and 21 cases satisfy (ii) and (iii), but not (i).

For each of the 25 cases identified using the above selection procedure, the detailed temporal evolution of the unsmoothed anomalous SLP index within the 7-pd period centered at \bar{O} was further scrutinized, so as to pinpoint the date at which the actual transition from a negative to a positive anomaly takes place. The pentad centered at this date is hereafter referred to as the “onset pentad” (T_o).

The representative spatial patterns of the anomalous SLP and vector wind associated with PSAC establishment are illustrated in Fig. 6 using shading and arrows, respectively. These charts are based on 25-case composites of the high-frequency (HF) component of the model fields, which is obtained by removing the LF component from the unfiltered values for each pentad. The composites have been constructed by grouping

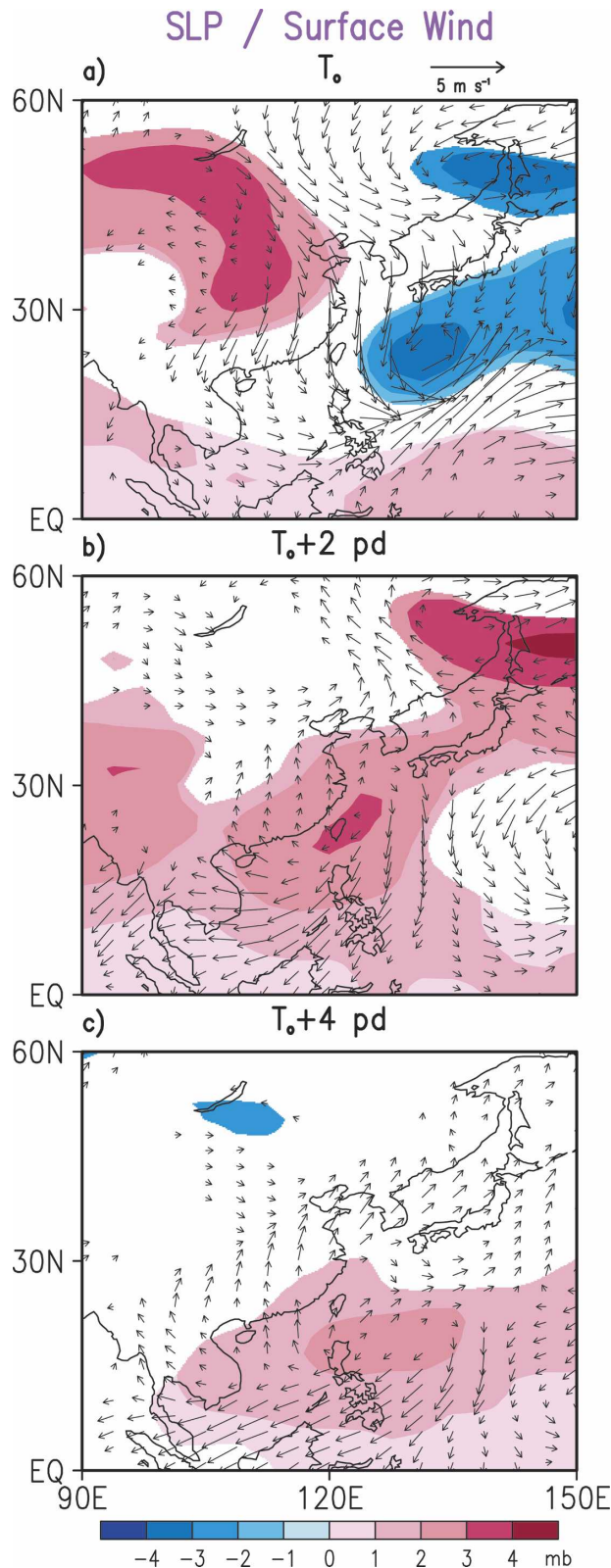


FIG. 6. Composites of the high-frequency component of SLP (shading; see scale bar at bottom) and surface wind vector (arrows; see scale at upper right) relative to the onset pentad T_0 of

data fields at various time lags relative to T_0 for individual cases. The distributions for the groups corresponding to T_0 , 2 pd after T_0 , and 4 pd after T_0 are displayed in Figs. 6a, 6b, and 6c, respectively.

At T_0 , the SLP pattern is dominated by a high pressure anomaly over the interior of the eastern Asian landmass and a low pressure center over the Philippine Sea (Fig. 6a). This configuration leads to strong pressure gradients and intense northerly flows over the eastern seaboard of China. The continental high pressure anomaly migrates southeastward with time, and arrives at the Philippine Sea about 4 pd after T_0 (Fig. 6c). At the latter stage, a clockwise flow pattern prevails in the vicinity of the newly established PSAC anomaly, with southerlies replacing the northerlies over East China seen earlier at T_0 . Some aspects of this synoptic development are reminiscent of those accompanying cold-air outbreaks over East Asia. The corresponding composites based on observational data (see Fig. 4 of WZ02) also indicate a continental origin for the PSAC anomaly, and a rapid reversal in the polarity of the SLP signal over the Philippine Sea in the onset phase.

The model results presented in this section suggest that the PSAC onset is linked to atmospheric variability on time scales of several pentad. The seasonal dependence of the air–sea coupling associated with such ISV, as well as the contributions of the observed ISV to the abruptness of PSAC establishment, have also been emphasized by WZ02. The following two sections are devoted to an assessment of the extent to which the observed relationships between ISV and PSAC development can be reproduced in the MLM experiment.

6. Principal modes of ISV in various seasons

The dominant space–time characteristics of the simulated ISV in the EAM region have been examined using extended empirical orthogonal functions (EEOF). A detailed description of this analysis tool has been given by Weare and Nasstrom (1982). In the present study, this technique has been applied to the HF component (see definition in section 5) of the standardized pentad means of SLP in the domain of 0°–40°N, 90°–180°. Horizontal variations are represented by a staggered grid mesh with zonal and meridional spacings of

← the PSAC anomaly, for (a) T_0 , (b) 2 pd after T_0 , and (c) 4 pd after T_0 . Composites have been performed over 25 cases in the GCM experiment for which the onset pentad can be clearly identified. Only SLP anomalies surpassing the 95% significance level are depicted by color shading.

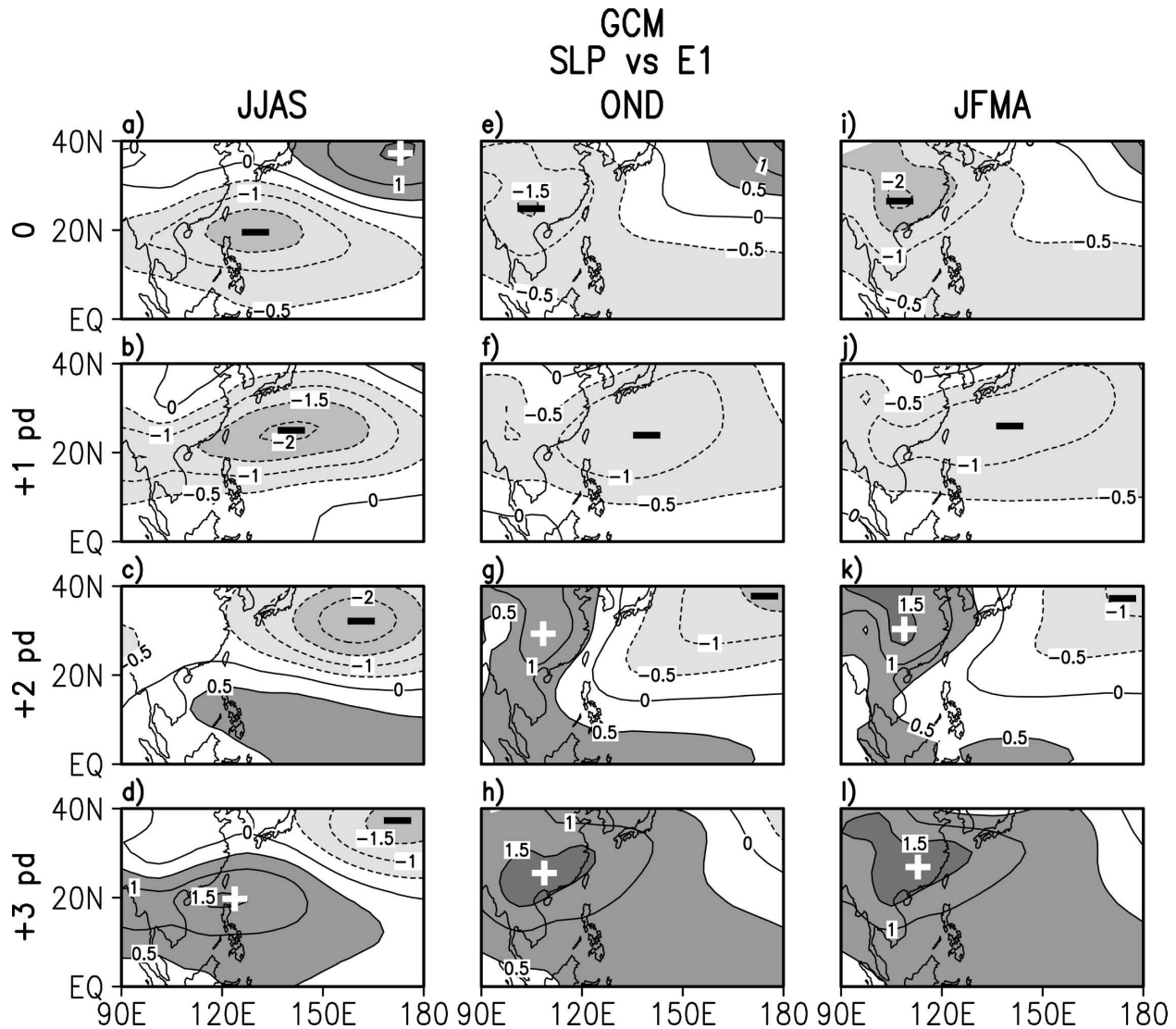


FIG. 7. Regression patterns of the high-frequency component of SLP vs the standardized temporal coefficients of the leading EEOF mode at lags of (top) 0, (second down) 1, (third down) 2, and (bottom) 3 pd. Results are shown for the (left) JJAS, (middle) OND, and (right) JFMA seasons. Contour interval: 0.5 mb. The EEOF analysis has been performed using GCM data for the SLP field.

15° and $\sim 9^\circ$, respectively. The total number of grid points is 232. The data record consists of all 73 pd in each of the 50 yr covered by the 16 individual integrations, so that it has a total length of $73 \times 50 \times 16 = 58\,400$ pd. The correlation matrix for the eigenanalysis has been constructed using temporal lags of 0, 1, 2, and 3 pd. The two leading eigenvectors, hereafter referred to as EEOF1 and EEOF2, explain 11.5% and 9.6% of the total variance, respectively.¹ This pair of vectors exhibit

a distinct spatial and temporal quadrature relationship with each other,² and collectively represent well-defined propagating phenomena. The nature of such traveling features is revealed in Fig. 7, which shows the space-time structure of EEOF1. These charts have been obtained by mapping the regression coefficients of the HF component of the SLP data at individual grid points versus the standardized time series of the expansion coefficients associated with EEOF1, with lags

¹ The fractions of variance explained by the third- to fifth-ranked eigenvectors (5.2%, 4.6%, and 4.5%, respectively) are considerably less than that accounted for by the leading pair.

² The time series of the expansion coefficients for EEOF1 and EEOF2 exhibit the strongest correlations (with absolute value of about 0.8) with each other at a lag of ± 1 pd.

ranging from 0 to 3 pd. The regression charts for the four individual lags are arranged along a column. Evolution of the characteristic patterns with time may be discerned by scanning each column from top to bottom. To delineate the seasonal dependence of the leading mode of variability, the lagged regression patterns have been computed using separate segments of the annual cycle. Results based on data for the JJAS, OND, and January–April (JFMA) periods are displayed in the left, middle, and right columns of Fig. 7, respectively. The corresponding regression pattern for the month of May, which is not included in the three periods considered here, bears a strong resemblance to the results for the JJAS season.

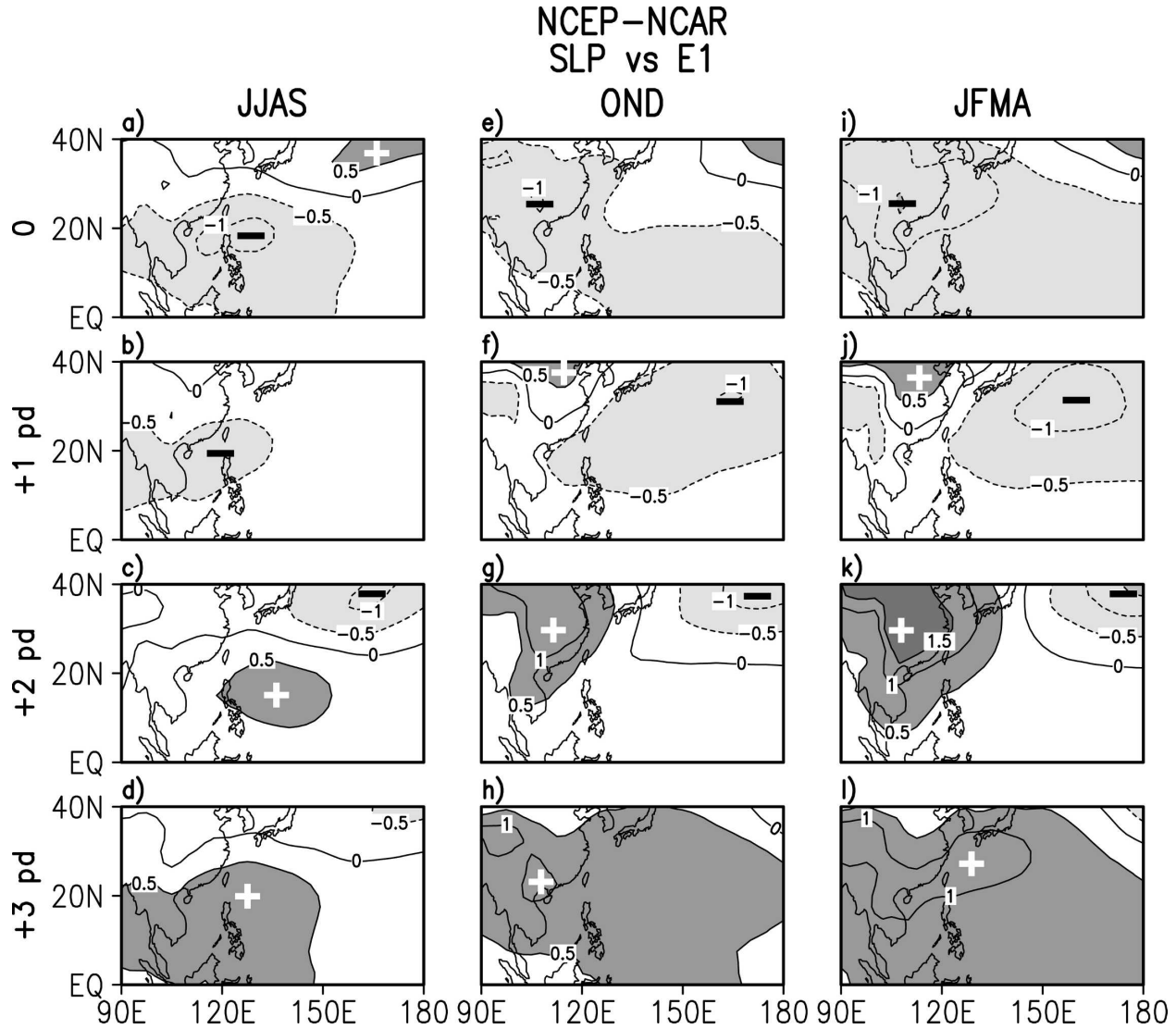
During the summer period, the leading mode is characterized by the development of a low SLP anomaly center over the South China and Philippine Seas (Fig. 7a). This feature subsequently migrates northeastward, and reaches the central North Pacific about 3 pd later (Fig. 7d). In Fig. 7c, a high pressure anomaly belt emerges over the western tropical Pacific. This feature travels northwestward to the South China and Philippine Seas 1 pd later (Fig. 7d). The out-of-phase relationship between the patterns in Figs. 7a and 7d is indicative of the cyclical nature of this evolution, with a typical half-period of about 3 pd. The regression patterns for temporal lags of 4, 5, and 6 pd (not shown) are similar to those for lags of 1, 2, and 3 pd, respectively, except for a sign reversal.

The regression charts for the boreal autumn and winter (middle and right columns of Fig. 7) are similar to each other, with amplitudes in the winter being relatively higher. A low SLP anomaly first appears over the East Asian landmass (Figs. 7e and 7i). It travels southeastward and approaches the subtropical western Pacific about 1 pd later. This feature then moves northeastward to the extratropical North Pacific, whereas the pattern over the Asian continent is replaced by a new high anomaly center (Figs. 7g and 7k). The half-period for this development is shorter than that in summer.

The fidelity of the simulation of the principal mode of ISV may be assessed by comparing the model patterns with their observational counterparts, shown in Fig. 8. The latter result has been obtained by applying the identical EEOF analysis to the SLP field in the NCEP–NCAR dataset for the 1950–99 period. The leading pair of eigenvectors for the observations, which explain 15.7% and 11.6% of the total variance, are also in quadrature with each other. The notable resemblance between Figs. 7 and 8 confirms that there is strong observational support for the characteristic evolution of the simulated SLP features associated with the primary ISV mode in various seasons.

Hsu (2005) has recently analyzed the preferred propagation of observed intraseasonal features of the summertime 850-mb vorticity field using lagged correlation techniques. His findings are indicative of prevalent northwestward migration from the equatorial western Pacific to the South China Sea region. This behavior is in accord with the evolution of the simulated positive SLP features appearing in Figs. 7c–7d. Unpublished results by the same author for the winter season also reveal southeastward migration of observed SLP features from the interior of the Asian continent to the South China coast, and northeastward movement from the latter zone to the North Pacific. These characteristics are consistent with the model charts presented in Figs. 7e–7l.

Some resemblance is evident between the simulated features associated with EEOF1 for the OND period (middle column of Fig. 7) and the synoptic development during the onset of the PSAC anomaly (Fig. 6). In particular, both sets of patterns show that the high pressure signal over the Philippine Sea region has its origin over continental East Asia from 1–2 pd earlier. The temporal correspondence of the principal ISV mode with PSAC development is further substantiated by compositing the expansion coefficients of EEOF1 and EEOF2 for the model atmosphere (hereafter referred to as E1 and E2, respectively) relative to the onset pentad T_o . This procedure has been performed over the 25 cases in El Niño years for which well-defined PSAC onsets can be identified (see previous section). The resulting composite time series of E1 and E2 with reference to T_o are plotted in Fig. 9. The quadrature relationship between E1 and E2 is evident. The amplitude of these coefficients in the 5 pd prior to T_o is noticeably higher than that for the 10 pd after T_o , thus implying that the leading ISV mode is relatively more active before the onset of the PSAC. The time series for E1 exhibits a prominent maximum at $T_o - 2$ pd. The timing of this peak indicates that the evolution of the anomalous SLP field just prior to the onset bears a strong resemblance to that associated with the EEOF1 mode. Specifically, the representative SLP patterns at $T_o - 2$ pd, $T_o - 1$ pd, T_o , and $T_o + 1$ pd correspond closely to those displayed Figs. 7e, 7f, 7g, and 7h, respectively. It is particularly worth noting that the eigenvector pattern associated with T_o (i.e., Fig. 7g in the present context) is similar to the composite chart for T_o (see Fig. 6a). This comparison illustrates that the development of the SLP field during PSAC onset, as inferred from the EEOF analysis, matches well with that deduced from the composite method in the previous section.



The relationships between the simulated SLP modes shown in Fig. 7 with tropical convection over the Indo-Pacific basin have been investigated using lagged regression charts of the precipitation field versus E1 based on the MLM experiment. During the summer season, these patterns (not shown) are dominated by the well-defined northward migration of zonally elongated precipitation belts extending from about 90°E to the date line. Such model features bear a considerable resemblance to those associated with the leading mode of intraseasonal variability of the observed outgoing longwave radiation (OLR; an indicator of tropical precipitation), as documented by Lau and Chan (1986) and Mo and Nogues-Paegle (2005), among others. In the OND and JFMA seasons, large amplitudes of E1 are seen to be coincident with prominent eastward migra-

tion of precipitation signals along the equator from the Indian Ocean to the western Pacific. These changes are reminiscent of the developments accompanying Madden–Julian oscillations in this sector, as described using OLR data by Lau and Chan (1985), Knutson and Weickmann (1987), and Mo and Nogues-Paegle (2005).³ In summary, the principal ISV mode of the model-generated SLP field is closely linked to organized patterns of convective activity in the deep Tropics. Many aspects of these simulated precipitation patterns are also discernible in the observed atmosphere.

³ In the model atmosphere, the near-equatorial precipitation features tend to have the same polarity throughout the Indo-western Pacific sector, whereas the corresponding observations indicate a dipole-like pattern in that region.

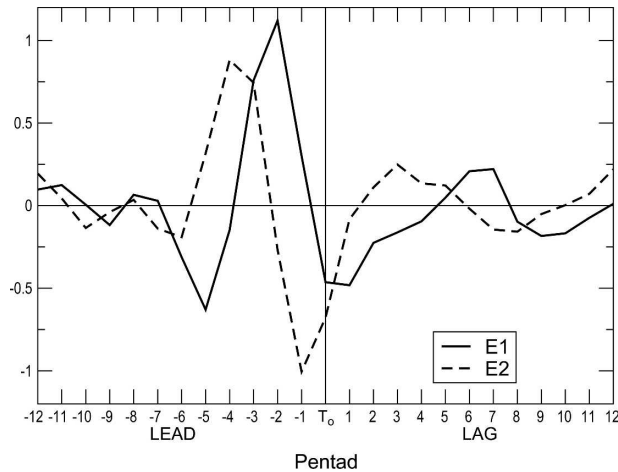


FIG. 9. Time series of the composites of the standardized temporal coefficients for the first pair of EEOF eigenvectors of the SLP field. Composites have been computed at various leads and lags relative to the onset pentad T_0 , and are based on 25 cases in the GCM experiment for which the PSAC onset can be clearly identified.

7. Air–sea interactions accompanying ISV

a. JJAS season

We now examine the influences of the background circulation on the atmosphere–ocean coupling associated with the leading summertime ISV mode. The prevalent large-scale flow pattern in the JJAS season is presented in Fig. 10, which shows the climatological distributions of the near-surface wind vector ($\bar{\mathbf{V}}$, arrows) and relative vorticity ($\bar{\zeta}$, contours) in the model atmosphere. The most prominent feature is the monsoon trough centered near 20°N and extending eastward from Indochina to about 150°E . The axis of this trough corresponds to a zonally oriented maximum in $\bar{\zeta}$

(contours in Fig. 10) and cyclonic turning of the wind vectors.

The nature of the air–sea feedbacks in the course of a half-cycle of the leading ISV mode in the JJAS season is delineated by the array of regression charts in Fig. 11. In analogy to the SLP patterns in Fig. 7, the panels along a given column in Fig. 11 are based on regression of a certain variable versus E1 at progressively increasing temporal lags. The variables chosen for this display include the surface wind vector (arrows in left column), wind speed (shading in left column), surface heat flux (middle column), and SST (right column). The HF component of the data for all 50 JJAS seasons in all 16 ensemble members of the MLM experiment has been used in this regression analysis. The surface heat flux includes the contributions of the radiative, sensible heat, and latent heat components, with positive anomalies corresponding to increased flux from the atmosphere to the ocean.

At zero lag, the leading ISV mode is characterized by a low pressure center (Fig. 7a) and a cyclonic wind pattern (arrows in Fig. 11a) over the PSAC region. Because this perturbation is embedded in the climatological monsoon trough (Fig. 10), the surface wind speed over much of the subtropical western Pacific is increased (shading in Fig. 11a). The enhanced wind speed is conducive to more heat loss in sensible and latent forms from the ocean to the atmosphere. The increased cloud cover accompanying the positive precipitation changes over the low pressure center (not shown) reduces solar heating of the ocean surface. Both factors contribute to a decrease of the energy transfer from the atmosphere to the ocean (Fig. 11e), and in turn to a lowering of the SST in the succeeding pentads (see right panels of Fig. 11). The cold SST perturbation attains maximum amplitude at about 2 pd (Fig. 11k) after the

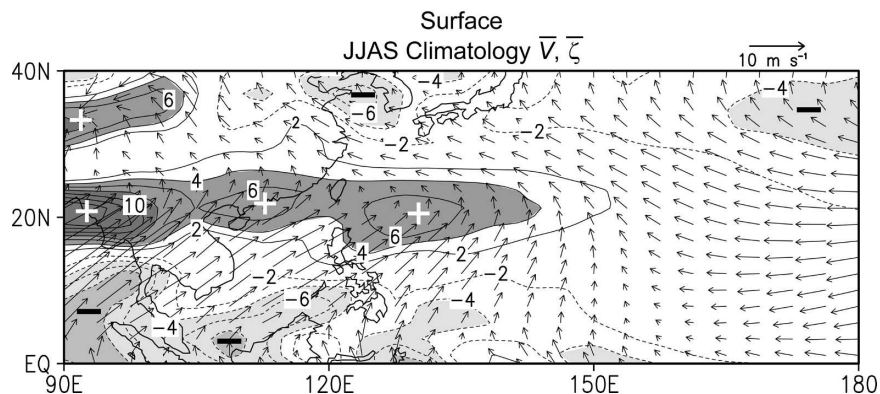


FIG. 10. Distributions in the model atmosphere of climatological surface wind vector (arrows; see scale at upper right) and relative vorticity (contours; interval: $2 \times 10^{-6} \text{ s}^{-1}$; zero contour not plotted) for the JJAS season.

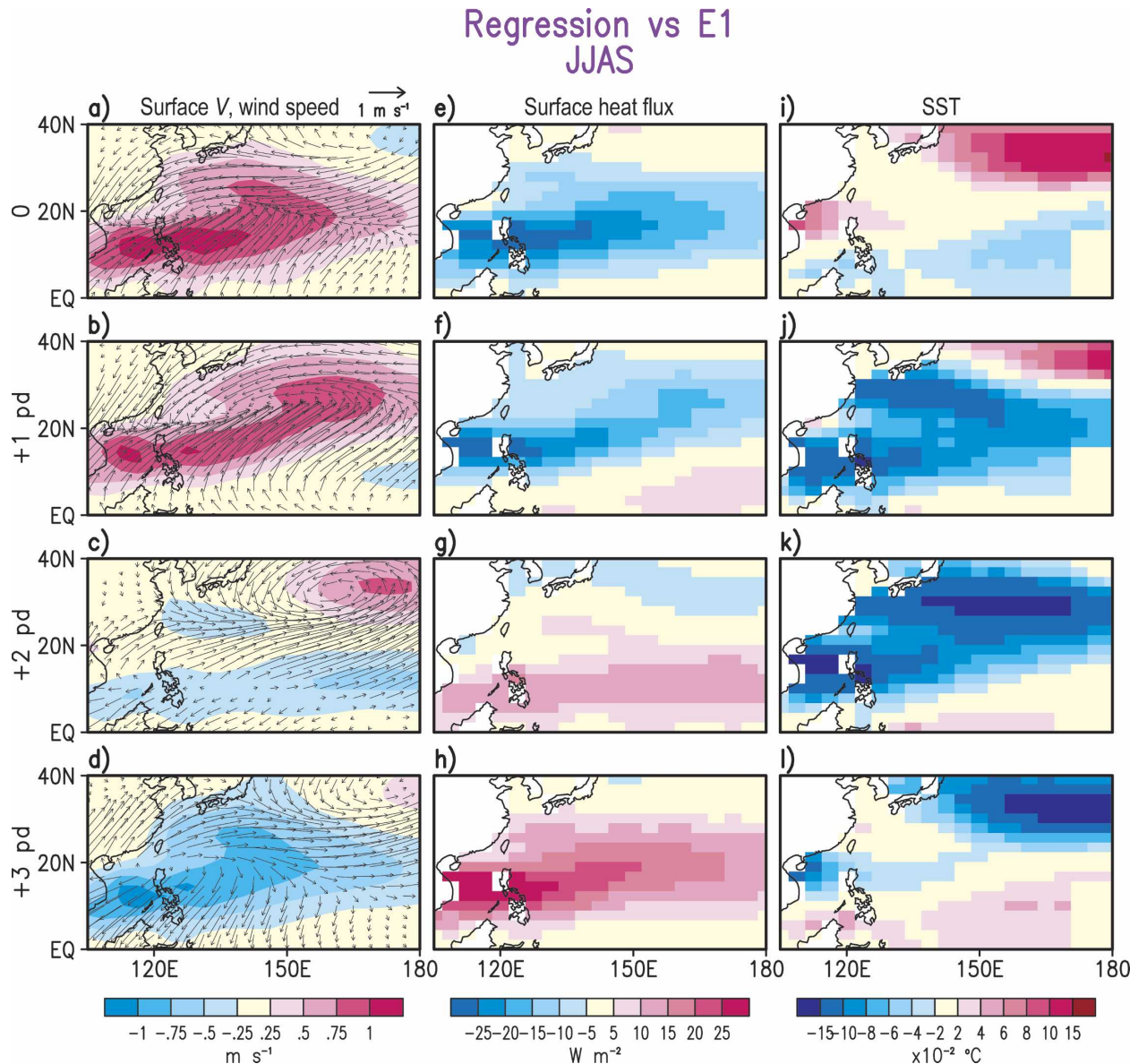


FIG. 11. Regression patterns of the high-frequency component of (left) surface wind vector (arrows; see scale at upper right) and wind speed (shading; see scale bar at bottom), (middle) total air-to-sea energy flux, and (right) SST vs the temporal coefficients of the leading EEOF of the SLP field at lags of (top) 0, (second down) 1, (third down) 2, and (bottom) 3 pd. All computations are based on GCM data for the JJAS season. The regression coefficients in the vicinity of the principal extrema in all panels generally exceeded the 99% significance level.

peak phase of the cyclonic signal (Fig. 11a). This negative SST anomaly is coincident with the emergence of an anticyclonic center over the subtropical western Pacific (Fig. 11c), which undergoes considerable amplification and northwestward displacement toward the Philippine Sea region in the following pentad (Fig. 11d). This anticyclonic development, which is primarily associated with the evolution of a dominant mode of ISV over the western subtropical Pacific (Figs. 7a–7d), is seen to be reinforced by the concurrent cold SST

anomaly that prevails in much of that region. The reduced wind speeds and cloud cover in this phase of the ISV are consistent with the increased atmosphere-to-ocean heat flux seen in Fig. 11h. The subsequent development of the coupled system in the remaining half of the ISV cycle may be inferred by reversing the polarity of all patterns shown in Fig. 11, and then scanning downward the charts in each column for a second time.

The model evidence presented in Fig. 11 suggests that, in the presence of a cyclonic time mean background

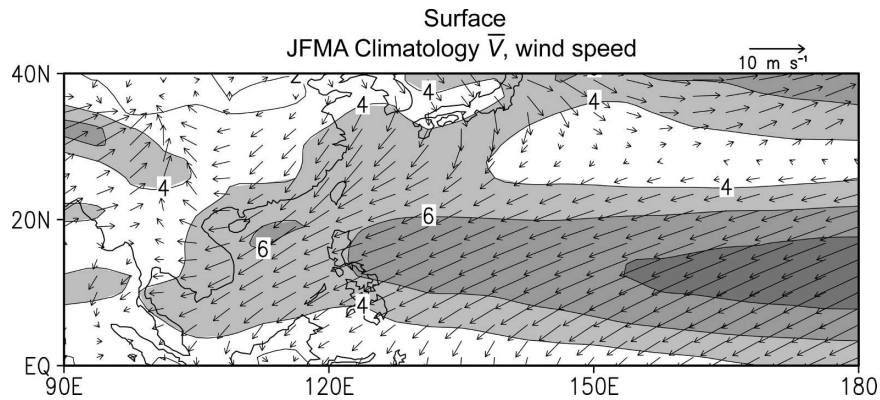


FIG. 12. Distributions in the model atmosphere of climatological surface wind vector (arrows; see scale at upper right) and wind speed (contours; interval: 2 m s^{-1}) for the JFMA season.

flow during the summer season, there exist positive feedbacks between atmospheric and oceanic perturbations associated with the leading ISV mode. This finding is in accord with the heuristic arguments put forth in WZ02 on the role of air–sea interaction in maintaining summertime ISV over the subtropical western Pacific.

Lagged regression charts analogous to those in Fig. 11 have also been constructed using data for the oceanic mixed layer depth (MLD). The results (not shown) indicate that the MLD anomalies are positively correlated with the local surface wind speed (shading in Figs. 11a–11d). Diagnosis of the SST tendency equation (e.g., see section 5 of Lau and Nath 2003) reveals that, in areas where the climatological surface heat flux is directed from the ocean to the atmosphere (as in the case of the Philippine Sea and parts of the South China Sea during summer), positive MLD changes lead to rising SST, and vice versa. Hence, the SST tendencies associated with MLD variations oppose the effects of anomalous surface heat fluxes (Figs. 11e–11h).

The spatial and temporal relationships between the simulated anomalies of surface wind, heat flux, and SST in the EAM region (Fig. 11) are similar to those associated with poleward-propagating convection bands over the Bay of Bengal on intraseasonal time scales, as reported in the observational and modeling studies of Sengupta et al. (2001), Vecchi and Harrison (2002), Rajendran et al. (2004), and Wang et al. (2005), among others.

b. JFMA season

The model climatology for the surface vector wind field (arrows) and wind speed (contours) for the JFMA season is shown in Fig. 12. The mean wintertime surface circulation is seen to be dominated by the northeasterly monsoon over the South China and Philippine Seas.

This pattern is in sharp contrast to the southwesterly flow in the summer regime (Fig. 10). Strong northeasterly trade winds also prevail over the subtropical western Pacific during the winter season.

The wintertime counterpart of the regression charts in Fig. 11 is presented in Fig. 13. The latter patterns have been computed using data for the JFMA period for all 50 available years. At zero lag, the arrival of a low SLP center at the East Asian seaboard (Fig. 7i) is associated with southwesterly surface wind anomalies off the southern Chinese coasts (see arrows in Fig. 13a). Because the orientation of these anomalies is opposite to that of the climatological flow field (Fig. 12), the wind speed is lowered in that region (shading in Fig. 13a). The weakened wind stirring in turn leads to reduction of heat loss from the ocean, so that positive heat flux anomalies prevail near the East Asian coasts (Fig. 13e). In conjunction with the anomalous pressure gradient pattern in the eastern half of the plotting domain of Fig. 7i, northeasterly wind perturbations are seen to prevail over the subtropical Pacific east of 130°E (Fig. 13a). The increased wind speeds enhance the surface heat loss in this region (Fig. 13e). Hence, the anomalous wind speed and heat flux patterns during winter (Figs. 13a and 13e) are characterized by much stronger east–west contrasts than the corresponding summertime patterns (Figs. 11a and 11e). These striking seasonal differences are primarily governed by the distinctive climatological wind patterns (i.e., monsoon trough in summer, northeasterly flow in winter) in which the ISV are embedded.

At a lag of 2–3 pd, the low SLP anomaly over China as described above is replaced by a high pressure center (Figs. 7k–7l). The attendant changes in the wind (Figs. 13c–13d) and surface heat flux (Figs. 13g–13h) are op-

Regression vs E1
JFMA

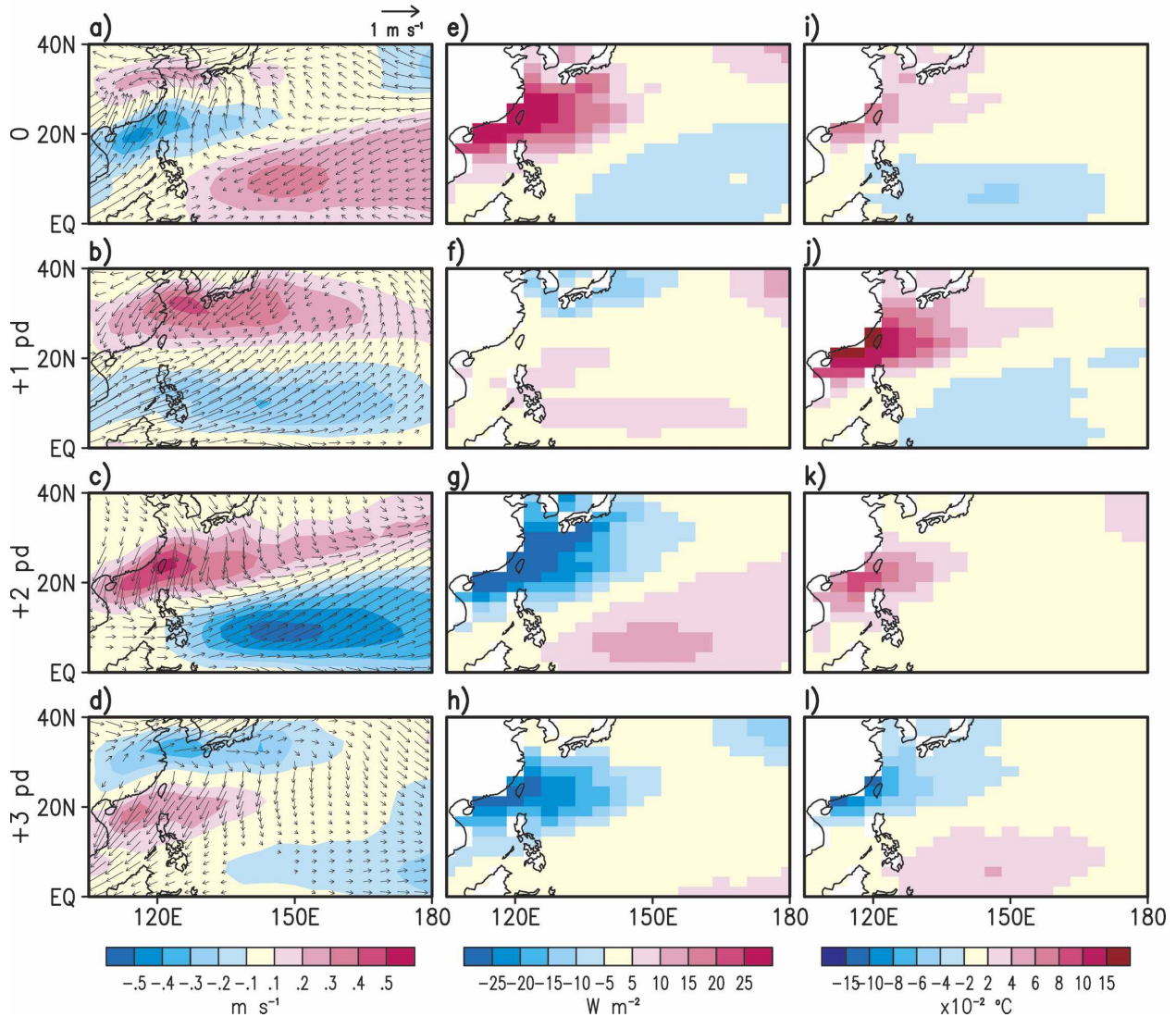


FIG. 13. As in Fig. 11, but for the JFMA season.

posite those occurring at zero lag. The distinctions between these wintertime results and the JJAS patterns for the corresponding ISV phase (Figs. 11d and 11h) are again evident.

The development of the SST field related to the leading ISV mode in the winter season (Figs. 13i–13l) closely follows that of the surface heat flux field (Figs. 13e–13h), with a temporal lag of about 1 pd. The timing of the SST evolution is such that the warm phase along the East Asian seaboard (Fig. 13j) is coincident with a low SLP center (Fig. 7j). Because a warm SST anomaly tends to reinforce cyclonic development, it would further strengthen the concurrent low pressure anomaly

and oppose the transition of this SLP signal to the high pressure phase of the ISV cycle. Analogously, the cold SST anomaly in Fig. 13l would enhance the persistence of the contemporaneous high pressure perturbation in Fig. 7l. The activities related to the leading ISV mode in the winter season are hence suppressed in the presence of air–sea feedbacks. These model findings on the modulation of wintertime ISV by air–sea coupling are consistent with the arguments presented by WZ02. As explained near the end of section 7a, the air–sea feedbacks associated with anomalous surface heat fluxes are partially offset by SST tendencies because of fluctuations of the depth of the oceanic mixed layer.

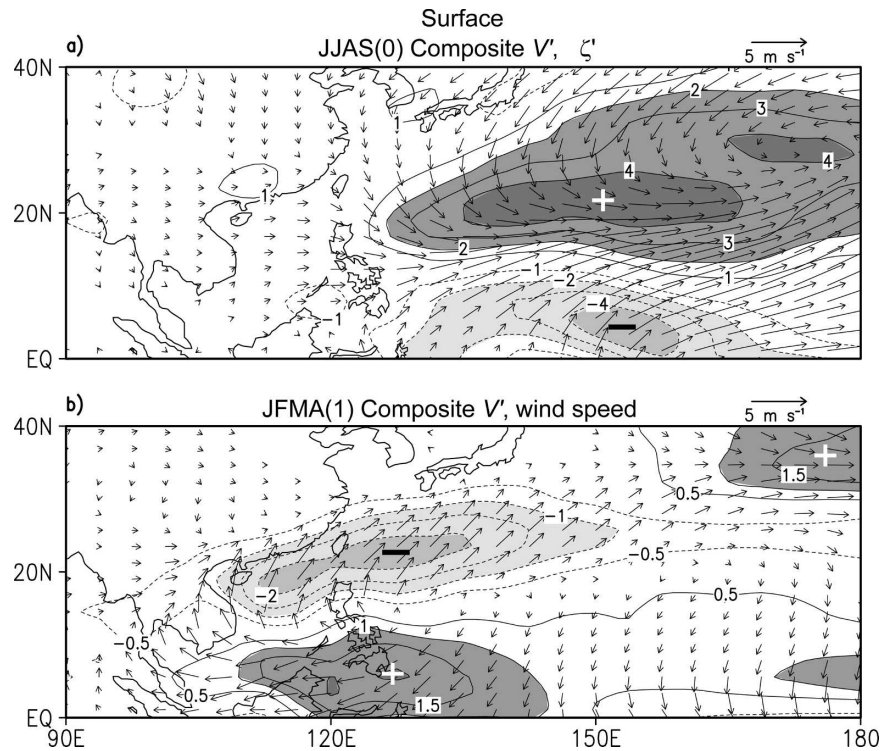


FIG. 14. Distribution in the model atmosphere of warm minus cold composites of the (a) surface wind vector (arrows; see scale at upper right) and relative vorticity (contours; interval: $1 \times 10^{-6} \text{ s}^{-1}$, zero contour not plotted) for the JJAS (0) period, and (b) surface wind vector (arrows; see scale at upper right) and wind speed (contours; interval: 0.5 m s^{-1} , zero contour not plotted) for the JFMA (1) period. The vorticity and wind speed anomalies in the shaded regions generally surpass the 99% significance level.

c. Modulation of ISV amplitude by ENSO during JJAS (0) and JFMA (1)

The evidence presented in sections 7a and 7b indicates that the basic state affects the behavior of ISV. Because the seasonally averaged circulation over the EAM region is modulated by ENSO-related forcing (see Wang et al. 2000; WZ02; and sections 3–4 of this paper), it is anticipated that ENSO variability would also exert some influence on the characteristics of ISV. Such relationships between ENSO and ISV activity are explored in this subsection.

We first summarize the salient changes in the basic state in the summer and winter seasons of ENSO events. The warm minus cold composites of the surface vector wind (arrows) and relative vorticity (contours) in the JJAS (0) phase of ENSO are displayed in Fig. 14a. The corresponding composites of the wind vector and wind speed fields in the JFMA (1) period are presented in Fig. 14b.

The summertime pattern in Fig. 14a is dominated by the cyclonic anomaly over the North Pacific. As ex-

plained in section 4, this feature is primarily a response to the ENSO forcing over the equatorial central Pacific. Comparison between Fig. 14a and the corresponding climatological pattern (Fig. 10) reveals that the cyclonic anomaly tends to strengthen the eastern portion of the climatological monsoon trough, and to extend this trough farther eastward or northeastward to the central Pacific.

The wintertime pattern in Fig. 14b indicates that the establishment of the PSAC is accompanied by anomalous southwesterly flow to the north and west of the anticyclonic center. Such wind perturbations are directed against the climatological wind pattern (Fig. 12) and result in a reduction of the local wind speed (contours in Fig. 14b). Conversely, the northeasterly wind anomalies to the south of the PSAC are parallel to the mean circulation, so that the surface wind speed is enhanced in those sites.

We next turn our attention to the ISV intensity during warm and cold ENSO events. The amplitude A of the leading ISV mode, as identified by EEOF analysis, has been computed as the square root of $(E1^2 + E2^2)/2$

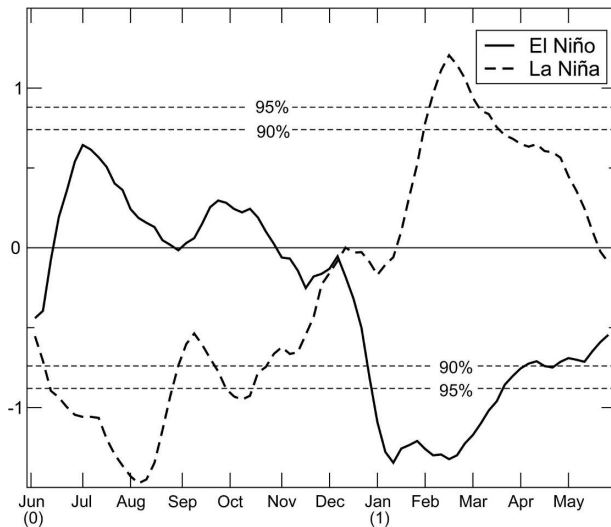


FIG. 15. Time series of the warm (El Niño) and cold (La Niña) composites of the anomalous amplitude of the leading EEOF mode for the SLP field in the model atmosphere. Threshold values at the 90% and 95% significance levels are indicated by dashed lines.

(see definition in section 6). The time series of the warm and cold composites of A (with seasonal climatology removed, and with 7-pd running mean smoothing applied) from Jun (0) through May (1) are plotted separately in Fig. 15. The horizontal dashed lines indicate threshold values at the 90% and 95% significance levels. During El Niño events, the amplitude of the leading ISV is typically above normal in the boreal summer and early autumn of Year (0), and below normal in the following winter and spring. The polarity of these changes in A is reversed in La Niña events, with reduced ISV activity through much of Year (0), and increased amplitudes thereafter.

A possible contributing factor to the enhancement of the leading ISV mode during the summer of El Niño years is the formation of the ENSO-induced cyclonic anomaly over the North Pacific, which serves to strengthen and expand the eastern portion of the climatological monsoon trough (see Figs. 10 and 14a). Because this mean flow feature facilitates positive feedbacks between the ISV activity in the atmosphere and SST changes in the ocean resulting from surface heat fluxes (see section 7a), its intensification and eastward extension toward the western subtropical Pacific would lead to even more active air–sea coupling, thus increasing the ISV amplitude. Conversely, the weakened quasi-stationary monsoon trough during the summer of La Niña events (Figs. 2b and 2d) is accompanied by reduced air–sea feedbacks and below-normal amplitudes of ISV activity (Fig. 15).

The primary SLP signals associated with the leading ISV mode in winter originate over the East Asian landmass (see Figs. 7i–7l). The impacts of air–sea interactions on the wintertime ISV activity, as described in section 7b, would be weaker than those discerned in the summer season. There exist strong similarities between the evolution of the wintertime ISV mode and that of cold-air outbreaks over the East Asian seaboard (e.g., Chan and Li 2004). Particularly noteworthy are the southeastward migration of the high SLP anomaly from the continental interior to the South China coast (Figs. 7k–7l), and the above-normal northeasterly surface winds over the South China and Philippine Seas (Figs. 13c–13d). The intensity and frequency of these episodes of cold-air surges are closely linked to the strength of the seasonally averaged winter monsoon flow in this region. During El Niño winters, the climatological northeasterlies over subtropical East Asia are weakened in the presence of the PSAC anomaly (Figs. 12 and 14b). The reduced cold-air activities and ISV amplitudes in these winters (Fig. 15) are in accord with the attenuation of the background monsoon circulation. On the other hand, the enhanced winter monsoon flows in La Niña episodes are coincident with stronger ISV perturbations.

The observed variations of the amplitude of the principal ISV mode have been examined by plotting the counterpart of Fig. 15 using coefficients of E1 and E2 based on NCEP–NCAR reanalysis data (Fig. 8). The observed evolution of A (not shown) is rather noisy and much less definitive than the model results. Further study is needed to assess the realism of the simulated changes in A during ENSO events. Such efforts are hampered by the lack of sampling of observed ISV activity during the limited number of ENSO events, because the observational datasets provide information on only one realization for each event, whereas 16 realizations are available from the ensemble experiment.

8. Discussion

The results presented in this paper on the atmospheric environment prior to and during the establishment of the PSAC anomaly in the summer and autumn of typical ENSO events are complementary to those reported earlier in LN04 on the maintenance of this anomaly in the following winter and spring. The cumulative findings in these two studies offer a complete description of the simulated atmosphere–ocean system in East Asia through the entire ENSO cycle (Fig. 2). In the boreal summer of Year (0) of El Niño events, the atmospheric circulation over East Asia is primarily modulated by the enhanced heating over the central

equatorial Pacific. This anomalous heat source forces a low-level cyclone anomaly over the North Pacific (Fig. 4), which in turn leads to temperature tendencies through advective processes (Fig. 5). These atmospheric changes give rise to a favorable setting for the initiation of the PSAC anomaly in the ensuing months. On the other hand, the diagnostics performed in LNW04 illustrate that, after the PSAC anomaly is established, it is reinforced by the Rossby wave response to the cold source situated over the western equatorial Pacific (see Fig. 7c of LNW04). These model results indicate that individual stages of PSAC development may be attributed to different facets of the ENSO-related forcing. Specifically, the incipient phase is influenced by heating over the central equatorial Pacific, whereas the mature phase is linked to cooling over the western Pacific. Both the warm and cold sources are associated with the eastward displacement of the Walker circulation during El Niño.

The nature of the leading ISV mode in the East Asian sector is highlighted in the second half of this article, with emphasis on its seasonal dependence, coupling with the underlying ocean, and modulation by ENSO events through changes in the background circulation. There exists observational support for the fidelity of the simulated ISV mode (see Figs. 7 and 8, and empirical studies cited in section 6). The nature of air–sea interactions accompanying this mode in different seasons (Figs. 11 and 13) is also in accord with the heuristic arguments and observational diagnoses presented in WZ02. The mechanisms proposed in WZ02 are, strictly speaking, applicable to stationary atmospheric and oceanic anomalies. The extent to which their arguments are valid remains to be determined for the migratory features in the ISV mode identified in our present study. More investigations are also needed to ascertain the relative contributions of tropical and extratropical processes to the ISV mode, and to assess the impacts of the ENSO-induced changes in the large-scale flow pattern (Fig. 14) on the amplitude of the ISV mode.

In conducting this modeling study, we have taken advantage of the availability of altogether 16 independent realizations of the MLM experiment. The much larger sample size of the model output (as compared to the observations) has facilitated the identification of various phenomena of interest in the simulated atmosphere. In particular, the synoptic features accompanying the PSAC onset (Fig. 6), as well as the space–time characteristics of, and air–sea interactions associated with, the leading ISV mode (Figs. 7, 9, 11, 13, and 15) have all benefited from the enhanced sampling of the pertinent signals. The model experiment has also pro-

vided certain data fields (such as heat fluxes at the air–sea interface, as analyzed in Figs. 11 and 13) for which observational estimates are not readily available. By exploiting such advantages of the GCM datasets, it is feasible to improve our understanding of the observed relationships between ENSO and the East Asian climate. In view of the ability of the GCM to capture some of the observed characteristics of the East Asian monsoon fluctuations associated with ENSO, the model output could be used with some confidence to test different hypotheses on the mechanisms contributing to ENSO–monsoon covariability, as proposed in previous empirical studies. By making use of the present experiment design, we have identified the role of ENSO-related SST forcing in setting up a summertime environment that is conducive to PSAC formation in the following autumn. We have also demonstrated the differing impacts of atmosphere–ocean interactions on ISV activity in the presence of summer and winter basic states. It is envisioned that, by incorporating additional processes (e.g., full dynamical air–sea coupling), the GCM would also serve as an effective tool for investigating other pertinent issues, such as feedbacks of monsoon variability on ENSO evolution.

While drawing inferences from the output of the MLM experiment, one must bear in mind various model biases. For instance, the degree of summertime interactions between ISV and the ocean in the western subtropical Pacific sector (Figs. 10, 11, and 14a) might be overly emphasized in this experiment, because of the excessive strength of both the climatological low-level monsoon trough (Figs. 1c–1d of LNW04) and the SLP anomaly during the summer of Year (0) (Fig. 2) in the model atmosphere. Another noteworthy discrepancy between model simulation and observation is the geographical distribution of the Madden–Julian oscillations in the deep Tropics, as well as the phasing between perturbations of SLP, convection, and surface fluxes associated with this phenomenon (Hendon 2000). These issues would have implications on the fidelity of the simulation of subtropical ISV examined in the present work.

Acknowledgments. We are grateful to Bin Wang for many stimulating discussions throughout the course of this study. We also thank Hailan Wang for performing the SWM calculations shown in Fig. 4, John Lanzante for conducting the MLM experiment, Huang-Hsiung Hsu for sharing his observational results on the propagation characteristics of ISV in the East Asian Monsoon region, as well as Chih-Pei Chang, Xianan Jiang, Gabriel Vecchi, Qin Zhang, and the official reviewers for offering constructive comments on previous ver-

sions of the manuscript. The NCEP–NCAR reanalysis data were provided by the NOAA–CIRES ESRL/PSD Climate Diagnostics Branch, Boulder, Colorado.

REFERENCES

- Alexander, M. A., and J. D. Scott, 1995: *Atlas of Climatology and Variability in the GFDL R30S14 GCM*. CIRES, University of Colorado, 121 pp.
- , —, and C. Deser, 2000: Processes that influence sea surface temperature and ocean mixed layer depth variability in a coupled model. *J. Geophys. Res.*, **105**, 16 823–16 842.
- Broccoli, A. J., and S. Manabe, 1992: The effects of orography on midlatitude Northern Hemisphere dry climates. *J. Climate*, **5**, 1181–1201.
- Chan, J., and C. Li, 2004: The East Asia winter monsoon. *East Asian Monsoon*, C.-P. Chang, Ed., World Scientific Series on Meteorology of East Asia, Vol. 2, World Scientific, 54–106.
- Chang, C.-P., Ed., 2004: *East Asian Monsoon*. World Scientific Series on Meteorology of East Asia, Vol. 2, World Scientific, 564 pp.
- , Y. Zhang, and T. Li, 2000a: Interannual and interdecadal variations of the East Asian summer monsoon and tropical Pacific SSTs. Part I: Roles of the subtropical ridge. *J. Climate*, **13**, 4310–4325.
- , —, and —, 2000b: Interannual and interdecadal variations of the East Asian summer monsoon and tropical Pacific SSTs. Part II: Meridional structure of the monsoon. *J. Climate*, **13**, 4326–4340.
- Gaspar, P., 1988: Modeling the seasonal cycle of the upper ocean. *J. Phys. Oceanogr.*, **18**, 161–180.
- Gill, A. E., 1980: Some simple solutions for heat-induced tropical circulation. *Quart. J. Roy. Meteor. Soc.*, **106**, 447–462.
- Gordon, C. T., and W. F. Stern, 1982: A description of the GFDL global spectral model. *Mon. Wea. Rev.*, **110**, 625–644.
- Hendon, H. H., 2000: Impact of air–sea coupling on the Madden–Julian oscillation in a general circulation model. *J. Atmos. Sci.*, **57**, 3939–3952.
- Hoerling, M. P., A. Kumar, and M. Zhang, 1997: El Niño, La Niña, and the nonlinearity of their teleconnections. *J. Climate*, **10**, 1769–1786.
- Hsu, H. H., 2005: East Asian Monsoon. *Intraseasonal Variability in the Atmosphere–Ocean Climate System*, W. K. M. Lau and D. E. Waliser, Eds., Praxis, 63–94.
- Huang, R., G. Huang, and Z. Wei, 2004: Climate variations of the summer monsoon over China. *East Asian Monsoon*, C.-P. Chang, Ed., World Scientific Series on Meteorology of East Asia, Vol. 2, World Scientific, 213–268.
- Kang, I., 2004: Current status of AGCM monsoon simulations. *East Asian Monsoon*, C.-P. Chang, Ed., World Scientific Series on Meteorology of East Asia, Vol. 2, World Scientific, 301–331.
- Knutson, T. R., and K. M. Weickmann, 1987: 30–60 day atmospheric oscillations composite life cycles of convection and circulation anomalies. *Mon. Wea. Rev.*, **115**, 1407–1436.
- Lau, K.-M., and P. H. Chan, 1985: Aspects of the 40–50 day oscillation during the northern winter as inferred from outgoing longwave radiation. *Mon. Wea. Rev.*, **113**, 1889–1909.
- , and —, 1986: Aspects of the 40–50 day oscillation during the northern summer as inferred from outgoing longwave radiation. *Mon. Wea. Rev.*, **114**, 1354–1367.
- , K. M. Kim, and J.-Y. Lee, 2004: Interannual variability, global teleconnection, and potential predictability associated with the Asian summer monsoon. *East Asian Monsoon*, C.-P. Chang, Ed., World Scientific Series on Meteorology of East Asia, Vol. 2, World Scientific, 153–176.
- Lau, N.-C., and M. J. Nath, 2000: Impact of ENSO on the variability of the Asian–Australian monsoons as simulated in GCM experiments. *J. Climate*, **13**, 4287–4309.
- , and —, 2003: Atmosphere–ocean variations in the Indo-Pacific sector during ENSO episodes. *J. Climate*, **16**, 3–20.
- , and B. Wang, 2006: Interactions between the Asian Monsoon and the El Niño/Southern Oscillation. *The Asian Monsoon*, B. Wang, Ed., Praxis, 479–512.
- , M. J. Nath, and H. Wang, 2004: Simulations by a GFDL GCM of ENSO-related variability of the coupled atmosphere–ocean system in the East Asian Monsoon region. *East Asian Monsoon*, C.-P. Chang, Ed., World Scientific Series on Meteorology of East Asia, Vol. 2, World Scientific, 271–300.
- Li, C., 1990: Interaction between anomalous winter monsoon in East Asia and El Niño events. *Adv. Atmos. Sci.*, **7**, 36–46.
- Manabe, S., J. Smagorinsky, and R. F. Strickler, 1965: Simulated climatology of a general circulation model with a hydrologic cycle. *Mon. Wea. Rev.*, **93**, 769–798.
- , R. J. Stouffer, M. J. Spelman, and K. Bryan, 1991: Transient responses of coupled ocean–atmosphere model to gradual changes of atmospheric CO₂. Part I: Annual mean responses. *J. Climate*, **4**, 785–818.
- Matsuno, T., 1966: Quasi-geostrophic motions in the equatorial area. *J. Meteor. Soc. Japan*, **44**, 25–43.
- Mo, K. C., and J. Nogues-Paegle, 2005: Pan America. *Intraseasonal Variability in the Atmosphere–Ocean Climate System*, W. K. M. Lau and D. E. Waliser, Eds., Praxis, 95–124.
- Rajendran, K., A. Kitoh, and O. Arakawa, 2004: Monsoon low-frequency intraseasonal oscillation and ocean–atmosphere coupling over the Indian Ocean. *Geophys. Res. Lett.*, **31**, L02210, doi:10.1029/2003GL019031.
- Sengupta, D., B. N. Goswami, and R. Senan, 2001: Coherent intraseasonal oscillations of ocean and atmosphere during the Asian summer monsoon. *Geophys. Res. Lett.*, **28**, 4127–4130.
- Smith, T. M., R. W. Reynolds, R. E. Livezey, and D. C. Stokes, 1996: Reconstruction of historical sea surface temperature using empirical orthogonal functions. *J. Climate*, **9**, 1403–1420.
- Sumi, A., M. Kimoto, and X. Shen, 2004: Simulation studies of the Asian monsoon using the CCSR/NIES AGCM. *East Asian Monsoon*, C.-P. Chang, Ed., World Scientific Series on Meteorology of East Asia, Vol. 2, World Scientific, 332–353.
- Ting, M., and L. Yu, 1998: Steady response to tropical heating in wavy linear and nonlinear baroclinic model. *J. Atmos. Sci.*, **55**, 3565–3582.
- Vecchi, G. A., and D. E. Harrison, 2002: Monsoon breaks and subseasonal sea surface temperature variability in the Bay of Bengal. *J. Climate*, **15**, 1485–1493.
- Wang, B., and Q. Zhang, 2002: Pacific–East Asian teleconnection. Part II: How the Philippine Sea anomalous anticyclone is established during El Niño development. *J. Climate*, **15**, 3252–3265.
- , and T. Li, 2004: East Asian Monsoon–ENSO interactions. *East Asian Monsoon*, C.-P. Chang, Ed., World Scientific Series on Meteorology of East Asia, Vol. 2, World Scientific, 177–212.

- , R. Wu, and X. Fu, 2000: Pacific-East Asian teleconnection: How does ENSO affect East Asian climate? *J. Climate*, **13**, 1517–1536.
- , —, and T. Li, 2003: Atmosphere-warm ocean interaction and its impacts on the Asian-Australian monsoon variation. *J. Climate*, **16**, 1195–1211.
- , P. J. Webster, and H. Y. Teng, 2005: Antecedents and self-induction of active-break south Asian monsoon unraveled by satellites. *Geophys. Res. Lett.*, **32**, L04704, doi:10.1029/2004GL020996.
- Weare, B. C., and J. S. Nasstrom, 1982: Examples of extended empirical orthogonal function analyses. *Mon. Wea. Rev.*, **110**, 481–485.
- Zhang, R., A. Sumi, and M. Kimoto, 1996: Impact of El Niño on the East Asian monsoon: A diagnostic study of the '86/87 and '91/92 events. *J. Meteor. Soc. Japan*, **74**, 49–62.